Lab on a Chip

Continuous flow actuation between external reservoirs in small-scale devices driven by surface acoustic waves

Michael B. Dentry,[a] James R. Friend[b] and Leslie Y. Yeo*[b]

We have designed and characterized a surface acoustic wave (SAW) fluid actuation platform that significantly improves the transmission of sound energy from the SAW device into the fluid in order to obtain enhanced performance. This is in distinct contrast to previous SAW microfluidic devices where the SAW substrate is simply interfaced with a microchannel without due consideration given to the direction in which the sound energy is transmitted into the fluid, thus resulting in considerable reflective and dissipative losses due to reflection and absorption at the channel walls. For the first time, we therefore demonstrate the ability for continuous fluid transfer between independent reservoirs driven by the SAW in a miniature device and report the associated pressure–flow rate relationship, in which a maximum flow rate of 100 μl min^{-1} and pressure of 15 Pa were obtained. The pumping efficiency is observed to increase with input power and, at peak performance, offers an order-of-magnitude improvement over that of existing SAW micropumps that have been reported to date.

1 Introduction

Transporting fluids in microfluidic devices, while apparently simple conceptually, is notoriously difficult to achieve, owing to the large capillary pressures and fluid resistance encountered at small scales, the former scaling inversely with the channel dimension and the latter to its fourth power.[1,2] Consequently, the majority of existing micropumping solutions[3–5] involve large and cumbersome bench-scale equipment such as capillary pumps for pressure-driven flow, signal generators and amplifiers for electrokinetic flow, or large rotational micromotors for centrifugation-driven flows (*e.g.*, the lab-on-a-CD platform[6])—acceptable perhaps for chip-in-the-lab platforms,[7] but still far from ideal if a truly miniaturized portable lab-on-a-chip device is to be realized.[8]

Surface acoustic wave (SAW) devices have been shown to enable a wide range of fast microfluidic actuation and manipulation,[9–14] in particular, driven by the powerful streaming generated in the fluid with an acoustic forcing that is concentrated over a small length scale.[15] Moreover, SAW transducers are simple, planar structures that are therefore easily fabricated at small scales, with feature sizes down to $O(100 \text{ nm})$, and are naturally suited to mass production: a single silicon or lithium niobate wafer can accommodate hundreds of transducers.[12] In contrast to other microfluidic

actuation methods, however, it is possible to drive the *entire* SAW microfluidic operation using a portable palmtop electronic driver circuit powered by a camera battery, which, together with the chip-scale transducer and fluidic channel, constitutes a portable handheld device. Another attraction of SAW devices is their ability to facilitate more complex microfluidic manipulation, permitting, for example, simultaneous electrical control of large numbers of fluid pathways and processes such as mixing[16] and interfacial deflection[17] within the small chip footprint, or in coupling with a superstrate.[18–20] For these reasons, SAW devices have been gaining considerable attention for small scale fluid actuation and manipulation in the microfluidic community of late.

The SAW device was first proposed as a means to actuate fluids by Shiokawa *et al.*,[21] wherein the SAW was found to generate high velocity streaming in liquids placed on the surface. A later study attempted to harness such streaming for use as a micropump, but the authors admitted that they were unable to do so, instead reporting it as a promising avenue for future development.[22] Aside from the ability for the SAW to enable sessile droplet transport[23,24] and advance liquid columns—both in channels[25–27] and on planar substrates,[28] it has recently been demonstrated that the acoustic streaming generated from SAW devices can also be harnessed for micropumping,[29,30] in which the SAW transducer was located at a point coinciding with a bend in a recirculating microchannel 'racetrack' loop. While demonstrative of the capability of the SAW for fluid actuation in a microchannel, the pump in such a closed-loop racetrack arrangement only

^{a} *Monash University, Clayton, VIC 3800, Australia*
^{b} *Micro/Nanophysics Research Laboratory, RMIT University, Melbourne, VIC 3000, Australia. E-mail: leslie.yeo@rmit.edu.au*

drives flow around a loop of fixed fluidic resistance, as opposed to the case of practical microfluidic applications, where fluid is typically transported through a microfluidic chip from one reservoir to another, both external to the microfluidic device, across a variable resistance posed by the channel. Moreover, in most studies, whether driven by SAW or by other mechanisms, the analysis of micropump performance is usually precluded by an inability to easily vary the load resistance, required to determine the power delivered by the pump as a function of flow resistance and characterized by the pressure–flow characteristics—the *pump curves*—common in macroscale pump studies.[3,31,32] Needless to mention, the pressure–flow relationships of SAW-based fluid pumps have yet to be reported in the literature.

In this study, we seek to demonstrate the first SAW fluid actuation platform capable of continuously transporting fluid through a device from one external reservoir to another independent reservoir and to characterize its behavior in terms of pressure and flow rate in response to a varied resistive load, so as to provide SAW pump performance characteristics that, to date, have not been documented. We utilize 3D printing to produce a novel pump design which interfaces the SAW device directly with the working fluid, avoiding the losses caused by reflection and absorption of SAW across coupling layers and through channel walls. In particular, the SAW device, through deliberate design, is aligned with the flow direction, and the device's dimensions were chosen to coincide with the attenuation of the sound beam emanating from the SAW substrate and the streaming jet it produces.[15]

2 Concept

Once in contact with a fluid, the SAW decays rapidly along the substrate it propagates, due to transmission of its energy into the fluid to produce propagating sound waves, here approximated as a sound beam emanating from the device at the Rayleigh angle, $\theta_R = \sin^{-1}(c/V_R)$; c is the speed of sound in liquid and $V_R = \lambda\omega/2\pi$ is the phase velocity of the SAW, in which $\omega/2\pi$ and λ are the center-frequency and wavelength of the SAW transducer, respectively. An acoustic forcing consequently arises that is distributed along the length of the beam and is related to the rate at which the acoustic energy is attenuated[33] along the beam axis. For power levels typical in SAW-based acoustic streaming, the acoustic force produces a momentum flux in the form of a streaming jet that emanates coaxially with the sound beam.[15]

The irradiation of the SAW energy into the fluid at the Rayleigh angle in the form of this sound beam is a very important consideration when designing efficient microfluidic devices given that it is the propagation of sound waves through this beam that gives rise to acoustic streaming in the fluid—the fundamental mechanism responsible for a large majority of SAW microfluidic operations.[9] Yet, and quite unfortunately, little (if any) attention has been paid to this consideration when designing SAW microfluidic devices. Consequently, the sound beam often propagates over the entire length of the microchannel
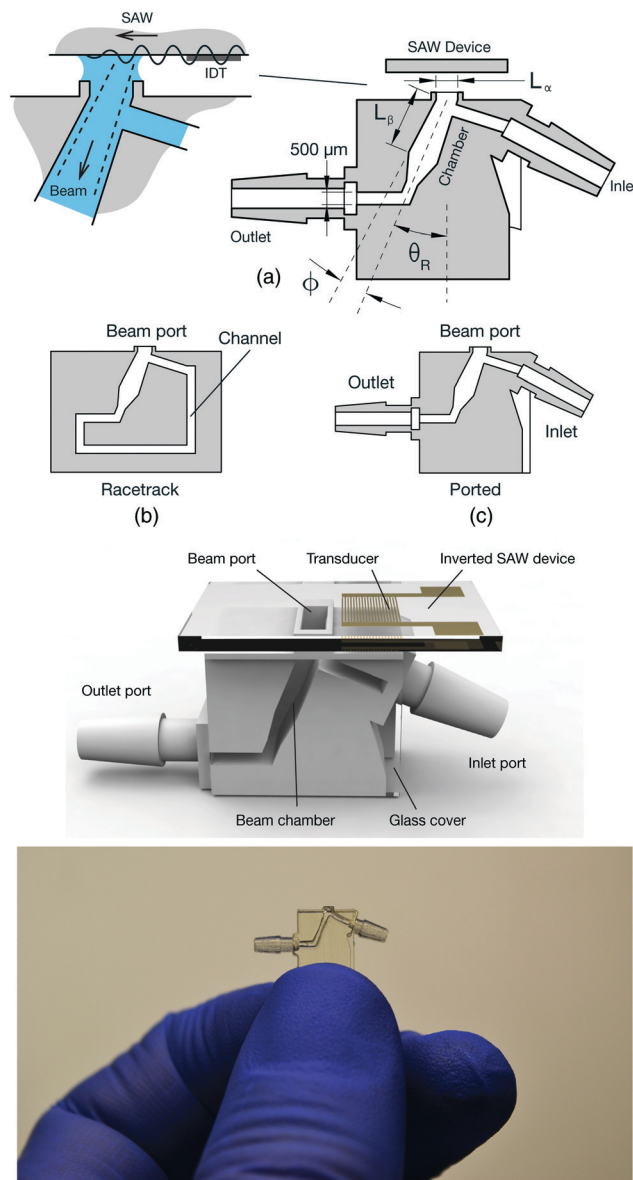

Fig. 1 (a) The pump design utilizes a chamber that is aligned with the axis along which the sound beam emanates from the substrate, defined by the Rayleigh angle θ_R, in order to efficiently harness the acoustic streaming and thus to generate a pressure differential across its length. The chamber is common to both (b) racetrack and (c) ported designs and expands slightly to account for the divergence of the beam, as indicated by the angle ϕ. The length of the racetrack channel is 17.5 mm and 32 mm for the 249 MHz and 122 MHz designs, respectively. An illustration (top) and an image (bottom) of the ported design are shown beneath. The latter shows the 3D-printed acoustofluidic chamber, constructed from UV-reactive polymer; after printing, a microscope coverslip was bonded to the front surface to enclose the chamber and the channels, as well as to form a viewing window.

height or width before it is able to fully attenuate. Rather, its energy is therefore absorbed or reflected by the channel wall, and hence the maximum streaming velocity that can be harnessed for microfluidic actuation is never fully attained. In some cases, the sound beam reaches the channel wall so rapidly before it attenuates that almost all of its energy is lost due to reflection and dissipation. In other cases, the SAW is transmitted through a microchannel wall or superstrate where its energy is also absorbed.

As such, the performance and efficiency of SAW devices to date have thus been significantly hampered.

In this work, we designed a series of pumps comprising a SAW transducer and an acoustofluidic beam chamber to capture and thus harness the energy of the sound beam and streaming jet. To maximize the acoustic energy available from the SAW and hence the sound beam to drive fluid flow, we sought to minimize reflections off the channel walls by aligning the chamber with the central axis of the beam, defined by θ_R, as illustrated in Fig. 1(a). For water at 20 °C on lithium niobate, which is the piezoelectric material the SAW substrate is composed of, $\theta_R = 22 \pm 2°$ (the 2° variation specified accounts for an estimated 70 °C (overly conservative for our experiments) increase in the fluid temperature and an 80 m s^{-1} difference in V_R measured across the range of operating frequencies employed), as verified from experiments utilizing similar SAW devices in a related study.[15] In addition, the chamber dimensions are designed such that its length accommodates the attenuation of the beam to 1% of its original amplitude to ensure that almost all of its energy is harnessed to drive fluid streaming. The pumps also utilize a liquid meniscus formed between the SAW device and the beam inlet to the chamber in order to transmit the sound beam directly into the chamber, therefore avoiding the need to transmit the wave through a solid substrate or under a lossy channel wall, as in previous work,[25,26,29] and thus eliminating losses associated with solid–liquid interfaces, reflection at the boundary, and dissipation during transmission through the solid media.

3 Experiment

The pump design utilizes a beam chamber with three openings, as shown in Fig. 2(a): the beam port, through which the sound beam enters, located at the top of the chamber; the outlet port, forming the 'discharge side' of the pump, located at the base of the chamber; and the inlet port, forming the 'suction side' of the pump, positioned as close to the beam port as possible. These inlet and outlet ports thus constitute the connection to the 'load' of the pump: either a racetrack channel arrangement connecting the two ports (Fig. 1(b)) or an arbitrary load between two independent reservoirs (Fig. 1(c)).

The chamber length is set at 13.8 mm for the 122 MHz SAW device and 3.4 mm for the 249 MHz device; the lengths were chosen such that they are equal to the length over which the amplitude of the sound wave, *i.e.*, the beam, reduces to 1% of the source amplitude. This length is given by $L = -\ln(0.01)/\beta$, where β is the frequency-dependent attenuation coefficient of the sound wave in the liquid. Defining X as the axis along which the beam propagates, the wave thus decays as $\exp(-\beta X)$.[15] While β is a function of many effects,[34] it can often be approximated as

$$\beta = \frac{b\omega^2}{2\rho c^3}, \tag{1}$$

where ρ is the density of the liquid and $b = \left(\frac{4}{3}\mu + \mu'\right)$, wherein μ and μ' are the shear and bulk viscosities of the liquid, respectively.[35]
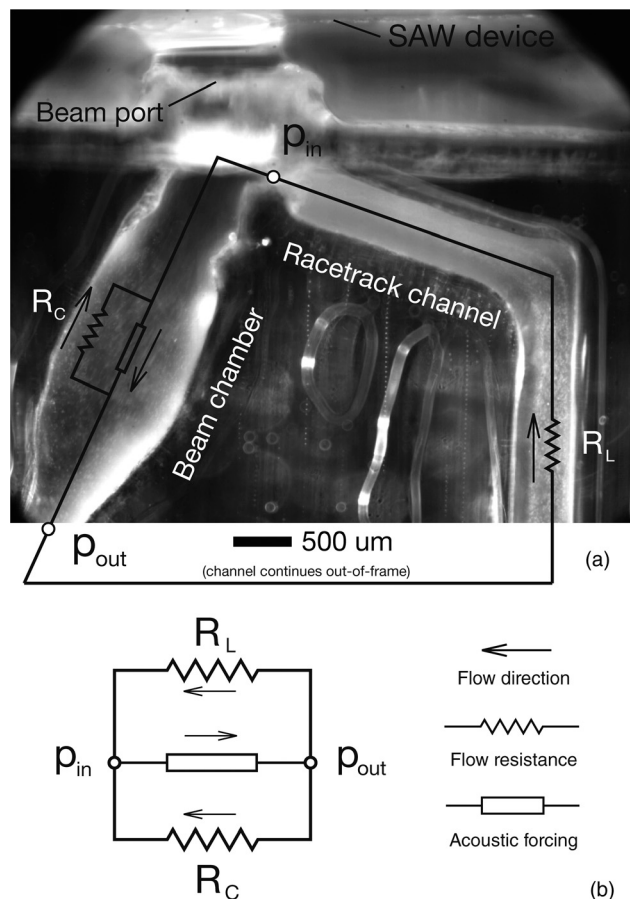

Fig. 2 (a) Side view of the pump in operation, showing a racetrack arrangement with a diverging wall profile. The SAW approaches from the right along the surface of the SAW device and decays on contact with the meniscus, generating a sound beam within the liquid that propagates along the Rayleigh angle θ_R through the beam port and into the beam chamber, thus giving rise to a streaming jet. The flow is driven around a fixed loop of length 32 mm and 17.5 mm for the 122 MHz and 249 MHz devices, respectively, forming the racetrack channel shown in panel (a) and Fig. 1(b). Mass is conserved by returning flow both along the racetrack and also within the beam chamber in the form of vortices—a division of flow governed by the respective resistance of each route, R_L or R_C, as depicted in panel (b).

The pumps are fabricated using a 3D-printer (Objet Eden260V™, Stratasys, Eden Prairie, MN, USA) out of a UV-reactive polymer (FullCure® 720, Stratasys, Eden Prairie, MN, USA), as shown in Fig. 1. In particular, the pump inlet port is located 200 μm from the beam port. The end of the beam chamber is narrowed to the 500 μm width of the channel, chosen for clear resolution of the flow velocity profile. In all cases, the channel is 3 mm deep, selected to match the aperture of the IDT. One side of the pump is left open so that a glass coverslip may be fixed in place using epoxy, creating a viewing window for observing the internal flow. During the experiments, the pump is fixed in a vertical position, with a camera aligned to capture the side view of the flow through the glass coverslip. The SAW device is inverted and suspended horizontally and lowered to make contact with the liquid at the beam port, as shown in Fig. 3. Once contact is
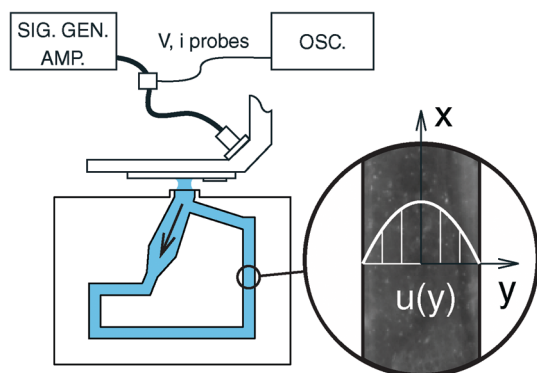
Fig. 3 Schematic depiction of the experimental setup for the racetrack configuration shown in Fig. 1(b). Also shown is a typical flow velocity profile, which was quantified visually at a point within the return leg of the racetrack channel.

made, a meniscus forms and the SAW device is retracted, maintaining the meniscus over a gap of approximately 500 μm. The center of the SAW transducer is aligned with the central plane of the pump using micropositioners and placed so that the liquid contact line is within 1 mm of the transducer.

Prior to each experiment, the beam chamber is first filled with deionized water, seeded with fluorescent microspheres of 5 μm diameter to aid flow visualization. A mercury light (Fiber-Lite MH-100, Dolan-Jenner, Boxborough, MA, USA) is used to illuminate the device and flow field. A high speed camera (FASTCAM SA5, Photron, Tokyo, Japan) is positioned perpendicular to the glass coverslip and records the acoustic streaming in the fluid at 125 frames per second. An electrical signal formed using a signal generator (SML-01, Rohde & Schwarz, Munich, Germany) and amplifier (10W1000C, Amplifier Research, Bothell, WA, USA) is delivered to the SAW device *via* an SMA cable, inducing a SAW on the device substrate, which, in turn, transmits its energy into the fluid in the form of a sound beam aligned with the Rayleigh angle, generating streaming within the beam chamber. Voltage (PP006A, LeCroy, Chestnut Ridge, NY, USA) and current (CT-1, Tektronix, Beaverton, OR, USA) probes are used to calculate the input power using an oscilloscope (WaveJet 334, LeCroy, Chestnut Ridge, NY, USA).

Characterizing the pump performance requires measurement of the pressure difference between the outlet and inlet, p, and the delivered flow rate, Q. The total power delivered by the pump is then $P = pQ$. While measurement of Q can be achieved visually, direct measurement of p can, however, be problematic at small scales and especially at low values—on the order of 10 Pa in SAW pumping.[29,30] We therefore utilize the method presented by Schmid *et al.* (2011) in which p is indirectly calculated from the velocity profile formed within a known channel geometry, assuming it to be purely pressure driven.[29]

We first designed the pump with a racetrack loop to characterize its steady-state behavior against a fixed flow resistance, shown in Fig. 1(b), in order to confirm that the assumption of pressure-driven flow is valid. The electrical signal is applied and acoustic streaming is generated within the pump chamber,

driving a continuous steady flow around the racetrack channel due to its fixed load resistance. The velocity profile across the central axis of the channel is recorded and analyzed using particle tracking software (Diatrack 3.01, Semasopht, Chavannes, Switzerland) to produce a series of particle velocity vectors corresponding to the particle displacements between frames.

To fully characterize the behavior of the pump, it must, however, be evaluated against a variable load so that the pressure–flow rate relationship can be measured. We thus designed a 'ported' pump with inlet and outlet ports that interface with flexible tubing (Clear C-FLEX, Cole Parmer, Vernon Hills, IL, USA) of 1.59 mm inner diameter, as shown in Fig. 1(c), which allowed connection to a variable load. The inlet and outlet ports are connected to independent reservoirs— beakers of 43 mm inner diameter—by 0.5 m of tubing, in order that the flow is driven between them, resulting in a slow level change. This level change is recorded at 60 frames per second using a video camera (Dino-Lite Pro, AnMo Electronics, New Taipei City, Taiwan) to calculate Q, which may then be used to estimate p by the method detailed in the next section.

4 Experimental results

We visually measured the velocity profile of the flow in the racetrack channel and established that the flow is pressure-driven by comparison with the theoretical prediction, using the experimental setup shown in Fig. 3. Particle tracking generates a velocity vector, $u(x,y,t)$, for each particle at time t; x and y correspond to the position along the width and length of the channel, respectively. The velocity field is created by dividing the region into a two-dimensional mesh of 50 μm square elements, defined by $u(x_i, y_i)$—equivalent to 10 elements across x and n elements along y—and averaging the velocity vectors within each element, producing the velocity field shown in Fig. 4(b). The average velocity profile across the channel is then computed by averaging velocities along y for constant x_i according to

$$u[x_i] = \frac{1}{n} \sum_{j=1}^{n} u[x_i, y_j],$$

producing the profile shown in Fig. 4(a).

For laminar flow in a rectangular channel driven by pressure gradient G, the velocity profile is given by[36]

$$u(y,z) = \frac{4G}{\mu w} \sum_{n=1}^{\infty} \frac{(-1)^{n+1}}{\beta_n^3} \left(1 - \frac{\cosh \beta_n z}{\cosh \beta_n (h/2)} \right) \cos \beta_n y, \quad (2)$$

where $\beta_n = (2n - 1)\pi/w$, with w being the channel width. Fitting eqn (2) with experimental data measured across the center of the channel at $z = 0$, z being the vertical axis, produces good agreement, as shown in Fig. 4 with $R^2 > 0.999$, supporting the contention that the flow is pressure driven and that the acoustic streaming in the racetrack channel outside of the beam chamber is negligible. On this basis, G is calculated from experimental measurement of the peak velocity, U_{max}. That the pressure gradient is assumed to be linear
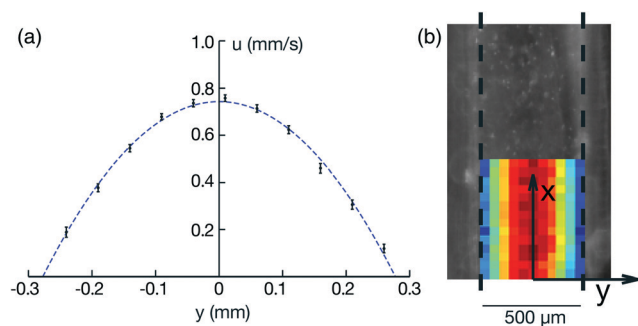
(a)

(b)

500 μm

Fig. 4 (a) Experimentally measured flow velocities across the central cross-section of the racetrack channel, which are used to generate (b) the velocity profile by means of eqn (2). Error bars refer to the standard error ($n > 30$). The dotted line corresponds to the theoretical velocity profile predicted by eqn (2), fitted using the pressure gradient G as a fitting parameter ($R^2 > 0.999$).

along the length of the racetrack channel implies a pressure difference between the inlet and outlet of $p \approx LG$. For each experiment, we calculate p using the measurement of U_{max}, and Q from the integration of eqn (2):

$$Q = \int_S u \, dA = \frac{8Gh}{\mu w} \sum_{n=1}^{\infty} \frac{1}{\beta_n^4} \left[1 - \frac{2}{\beta_n h} \tanh\left(\beta_n h / 2 \right) \right]. \quad (3)$$

The power delivered by the pump, $P = pQ$, is plotted in Fig. 5 against the input power, P_e, for the various racetrack arrangements. P is found to grow exponentially with an exponent greater than unity, implying that the pump efficiency increases with input power. The best performance was observed in the case of the short chamber, using a 122 MHz transducer, where the beam decay length was longer than the chamber length. In general, the 122 MHz device also performed better than the 249 MHz device; we however attribute this to the particular experimental setup employed: the device was suspended approximately 500 μm from the beam port in all cases—due to the longer decay length of the 122 MHz beam, approximately 27% of P_e is dissipated before the port, compared with 71% for the 249 MHz device. This results in the generation of streaming within the meniscus rather than in the pumping chamber where it is more
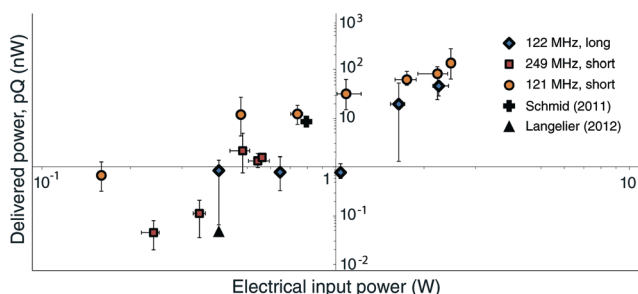
effectively harnessed. In the longer chamber, the reduction in performance of the 122 MHz device is likely due to the larger width of the beam chamber, which provided a low-resistance route for recirculation within the chamber to occur.

We vary the divergence angle of the beam chamber, ϕ (shown in Fig. 1(a)), between −5° and 5° to assess the effect of constraining the streaming within the chamber. Video footage was taken at 500 frames per second to resolve the particle motion: the flow within the chamber has a significantly higher velocity than in the channel. As before, the velocity field was constructed from the particle tracking results, from which the streamlines shown in Fig. 6 were produced. The streaming field appears to be vortical in nature, rotating about a point approximately halfway along the beam chamber. As the flow structure is similar for all cases, it follows that the parallel and converging chamber profiles pose high resistance to recirculation due to their constricted geometry, and therefore a larger proportion of energy is dissipated across the load of the pump. This is reflected in the pump velocity measured in the parallel case being a factor of 1.5 greater than in the diverging case.

We now discuss the results for the ported pump design schematically depicted in Fig. 1(c) to demonstrate pumping between independent reservoirs, quantified by the flow rate, $Q(t)$, and pressure, $p(t)$. The short chamber pump design was interfaced with the 122 MHz device and fixed according to the configuration shown in Fig. 7(a). Three separate power levels were applied and the height difference between fluid levels in the reservoirs, $h(t)$, was measured over time and plotted in Fig. 8(a); the flow rate is then $Q(t) = Ah'(t)/2$, where A is the cross-sectional area of each reservoir, and h' denotes the derivative of h with respect to t. We calculated the pressure $p(t)$ as a function of the gravitational pressure head developed between the reservoirs, which is directly proportional to $h(t)$ and the pressure difference caused by viscous dissipation, itself a function of $Q(t)$ and therefore $h(t)$. The total power delivered by the pump is quantified by $P(t) = p(t)Q(t)$; here, we show how measurement of $h(t)$ allows the calculation of $P(t)$, efficiency, and the pressure–flow rate relationship that governs the pump performance. The only source of significant experimental uncertainty is from the
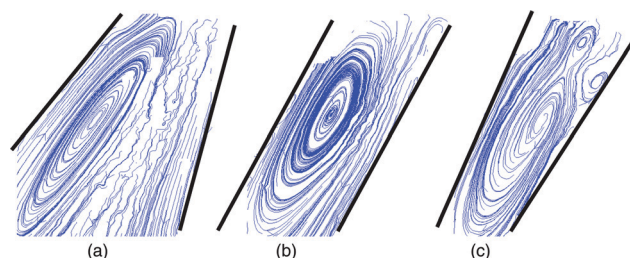

Fig. 5 Power delivered by the various racetrack pump designs and dissipated across the 'load' (i.e., the racetrack channel), equal to $P = pQ$ for various values of the electrical input power, P_e. Error bars correspond to the standard error ($n = 3$). The performance of previously reported racetrack pumps[29,30] is shown for comparison.

Fig. 6 Streamlines generated within the beam chamber for the 122 MHz device at constant input power, constructed by seeding the flow field with particles and tracking them in time over an average of 1000 frames of footage. The pumping flow rate produced by (a) the diverging profile was two-thirds the rate produced by (b) the parallel and (c) converging profiles.
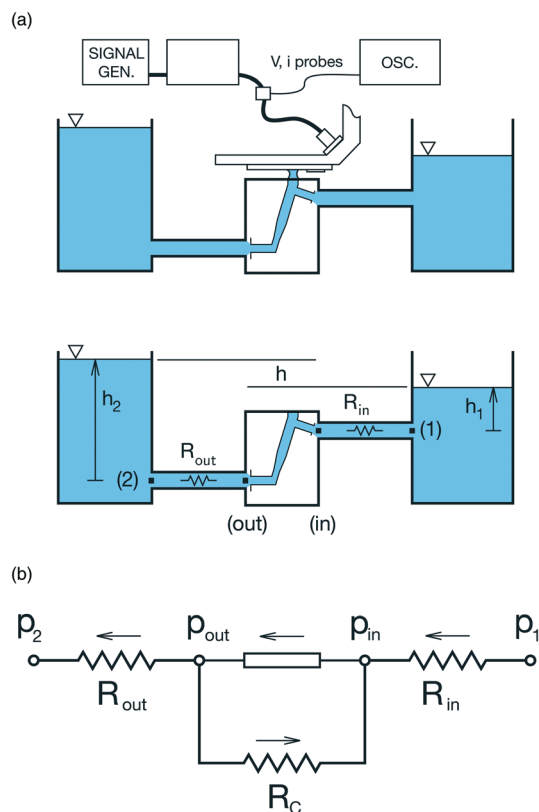
(a)

(b)

Fig. 7 Schematic depiction of (a) the ported pump design and (b) its associated resistive flow network. Flow is driven from one beaker to the other at constant power, while the differential height h is measured over time. As h increases, so does the adverse pressure gradient experienced by the pump, permitting its performance to be characterized over a varied load.

$$h(t) = \frac{p_0}{\rho g}(1 - e^{-\rho g t/C_0})$$
$$R^2 > 0.9999$$

(a)

$$Q(t) = (Ap_0/2C_0)e^{-\rho g t/C_0}$$
$$R^2 > 0.8632$$

(b)

$$p(t) = p_0 + p_0 e^{-\rho g t/C_0}\left(\frac{C}{C_0} - 1\right)$$
$$R^2 > 0.9864$$

(c)

Fig. 8 Evolution of (a) the differential height, h, (b) the flow rate between reservoirs, Q, and (c) the differential pressure, p, over time, under the application of a constant electrical power of 1.45 W to the SAW device. The solid lines are the theoretical predictions afforded by the models given by eqn (7), (8) and (9), respectively. Error bars correspond to the experimental uncertainty.

measurement of h, calculated from the average of the measured level changes at two different locations of the meniscus height, each with an uncertainty of ±1 pixel. Adding the two in quadrature, the combined uncertainty for h is equivalent to $\pm 1/\sqrt{2}$ pixels. This uncertainty is propagated through the calculation of p and Q, represented by the error bars in Fig. 8.

The pressure delivered by the pump, $p(t)$, is given by the differential pressure across the pump inlet and outlet, *i.e.*, $p = p_{out} - p_{in}$, shown in Fig. 7. This acts to drive flow along the two lengths of tubing and to counteract the gravitational pressure generated by the differential height of fluid, $h = h_2 - h_1$, as shown in Fig. 7(a). The pressure drop along the length of the tubing is characterized by a total resistance of $R = R_{in} + R_{out}$, such that the pressure drop across the tubing is given by $\Delta p = RQ$.

The differential pressure $p(t)$ is then given by

$$p(t) = RQ(t) + \rho g h(t) = \frac{RAh'(t)}{2} + \rho g h(t), \quad (4)$$

where R is the flow resistance along the tubing. We derive R on the basis that the flow generated by the pump is pressure-driven and laminar (since the Reynolds number Re ~ 1), confirmed in Fig. 4—Poiseuille flow—which dictates a flow resistance of
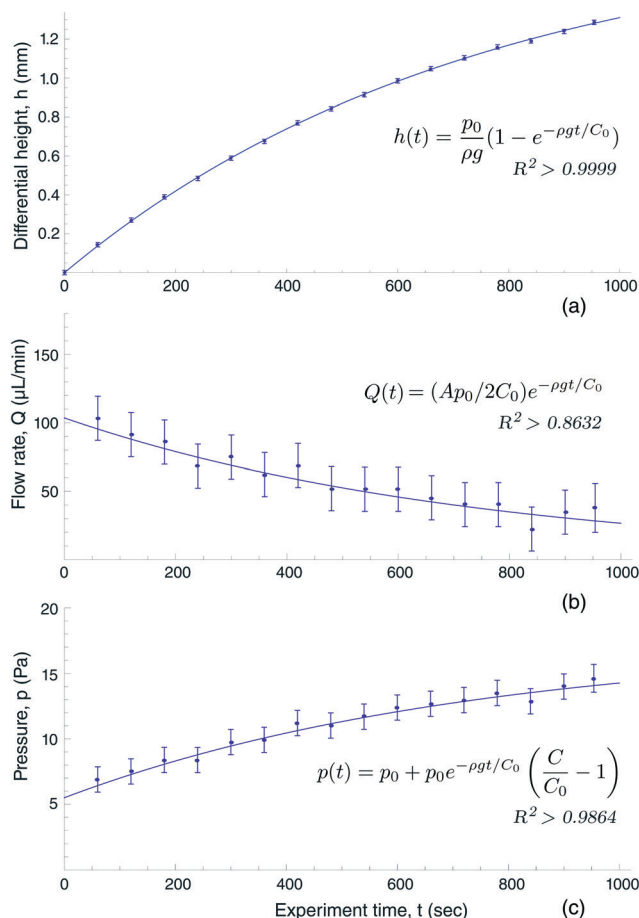
$$R = \frac{128\mu L}{\pi D^4}, \quad (5)$$

where L and D are the length and diameter of the tubing, respectively. The pressure delivered by the pump, $p(t)$, calculated by substitution of eqn (5) into eqn (4), is then plotted with $Q(t)$ in Fig. 8(b) and (c).

The pump curve—p *vs.* Q—shown in Fig. 9 reveals the inverse relationship typical of pump curves in general, corroborated by experimental data and thus confirming the existence of an optimal load at which the pump achieves maximum efficiency.

We now derive the relationship governing the pump curve. The change in fluid height, $h(t)$, is described by eqn (4), which has the following solution:

$$h(t) = \frac{e^{-\rho g t}}{C}\int_0^t e^{\rho g \tau} p(\tau) \, d\tau, \quad (6)$$

where $C = RA/2$ and τ is a dummy time variable: the unknown function $p(\tau)$ however precludes the existence of a closed-form
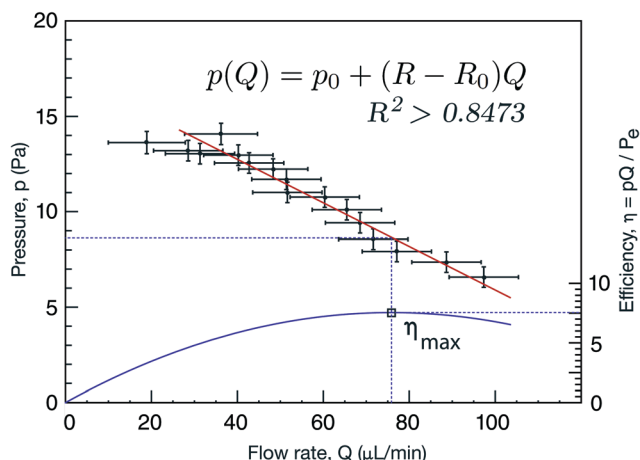
Fig. 9 The SAW 'pump curve', in which pressure, p, is given as a function of flow rate, Q. The data points are experimentally measured, with error bars corresponding to the experimental uncertainty. The solid line shows the theoretical prediction given by eqn (10) with a fit of $R^2 > 0.8473$. The dashed line denotes the efficiency of the pump, $\eta = P/P_e = pQ/P_e$: the linear $p(Q)$ relationship implies a parabolic $\eta(Q)$ relationship and thus a maximum operating efficiency, located at an optimal resistive load.

solution. Nevertheless, a solution may be obtained by assuming an *equivalent* constant pressure, *i.e.*, $p(\tau) = p_0$, thus rendering eqn (6) homogeneous:

$$h_0(t) = \frac{p_0}{\rho g}(1 - e^{-\rho g t/C_0}). \qquad (7)$$

Here, p_0 and C_0 are artificial parameters, related to the physical quantities by $p_0/C_0 = p(t)|_{t=0}/C$, providing a means to fit the theory to the experiment and avoiding the unknown function $p(\tau)$. The parameters p_0 and $C_0 = R_0A/2$ are varied to produce a least-squares fit of h_0 onto the experimental data, yielding an excellent fit ($R^2 > 0.9999$), as shown in Fig. 8(a). Substitution of $h_0(t)$ for $h(t)$ in eqn (4) then gives the pressure function required to produce eqn (7):

$$p(t) = p_0 + p_0 e^{-\rho g t/C_0}\left(\frac{C}{C_0} - 1\right), \qquad (8)$$

which may be substituted into eqn (6) to verify that $h(t) = h_0(t)$. The flow rate is then given by

$$Q(t) = (A/2)h'(t) = (Ap_0/2C_0)e^{-\rho g t/C_0}. \qquad (9)$$

These pressure and flow rate relationships are plotted against the experimental data in Fig. 8(b) and (c). Good agreement is obtained for the former ($R^2 > 0.9864$), although there is a lower coefficient of determination ($R^2 > 0.8632$) for the latter due to the error in differential height measurements at low flow rates.

The pump curve, or $p(Q)$ curve, may then be simplified to

$$p(Q) = p_0 + (R - R_0)Q \qquad (10)$$

and is plotted against the experimental data in Fig. 9. The relationship between p and Q is linear, which implies a

parabolic relationship between the delivered power and the flow rate: $p(Q)Q = p_0Q + (R - R_0)Q^2$. The pump efficiency, $\eta = pQ/P_e$, is plotted as the dashed line in Fig. 9; we observe a clear peak efficiency at $Q = p_0/2(R_0 - R)$ corresponding to an optimal load resistance. Under this condition, the pump delivered a pressure of $p = 16.5$ Pa at $Q = 95$ µl min^{-1} for an input power of $P_e = 1.81$ W, corresponding to a delivered power of $pQ = 26$ nW and a thermodynamic efficiency of $\eta = pQ/P_e = 1.48 \times 10^{-8}$.

5 Discussion

An important implication of the linear pressure–flow rate relationship in Fig. 9 is that the behavior of the acoustofluidic interaction within the beam chamber is reasonably unaltered by increases in the load resistance. In other words, the SAW-driven pump strategy that has been presented should maintain predictable operating behavior at constant input power relatively independent of variations to the resistive load.

Overall, the peak performance of the pump delivered a pressure of $p = 16.4$ Pa at $Q = 1.57$ ml min^{-1} and a total delivered power of $pQ = 0.43$ µW at an electrical input power of $P_e = 2.21$ W. This corresponds to a thermodynamic efficiency of $\eta = 1.94 \times 10^{-7}$—an order of magnitude improvement on the efficiency reported for an existing SAW pump at $p = 4.8$ Pa, $Q = 0.15$ ml min^{-1} and $P_e = 794$ mW.[29]

We have found that pumping efficiency increases significantly with input power, from $\eta \sim 10^{-10}$ at $P_e = 1.14$ W to $\eta \sim 10^{-8}$ at $P_e = 1.81$ W in the case of the ported pump. We postulate the efficiency increase to be due to a larger proportion of the flow being delivered to the load rather than recirculating within the beam chamber, on the basis of the higher shear gradients and increased jet momentum and length within the chamber, justified given that the pump may be represented as a resistive flow network which assumes a resistance, R_i, for each element of the pump. The network attributes a resistive loss to the shear gradients associated with the recirculating flow within the beam chamber, R_C; the primary jet, R_J; the input tubing, R_{in}; and the output tubing, R_{out}. R_C and R_J are complex functions of the acoustofluidic system, but R_{in} and R_{out} are constants, as established earlier. The flow network is shown for the case of the racetrack design in Fig. 2(b) and for the ported design in Fig. 7(b).

The pressure difference between the pump inlet and outlet also creates an adverse pressure gradient *within* the beam chamber, acting to confine the flow to the chamber itself, against or around the primary streaming jet, expending energy through viscous dissipation. This results in the division of the flow at the outlet: a proportion is delivered to the load and the remainder is returned to the inlet *via* recirculation within the chamber. This implies that the pump efficiency is linked to the ratio R_C/R_L and that the chamber should be designed such that $R_C \gg R_L$. The equivalent resistance to this return flow, R_C, is governed by the shear stress experienced during recirculation, suggesting that R_C is

maximized by increasing the jet flow rate or minimizing the cross-sectional area of the chamber, thus providing an explanation as to why increasing P_e, reducing the chamber dimensions, or narrowing the chamber walls all led to increased pump efficiencies in the experiment.

Designing the beam chamber such that the flow is laminar and does not separate from the wall—in other words, eliminating vortical recirculation—therefore theoretically maximizes the efficiency of the pump. Other authors have presented similar studies in the optimization of micro-diffusers.[37–39] Alternatively, generation of a turbulent jet occupying a large proportion of the channel may enforce purely unidirectional flow under certain conditions, limited by the angle of the wall profile.[40] These concepts are identified as potential areas of future development for increasing the performance of SAW pumps.

The meniscus used to transmit the sound beam from the SAW device into the beam chamber provides a near-lossless acoustic conduit compared to the solid materials constituting the channels that are in contact with or bonded to the SAW substrate in previous device conceptions.[25,26,29] It remains stable during operation for the input powers employed and does not advance or recede given that the acoustic streaming is predominantly (and through deliberate design) directed into the beam chamber. Evaporation at the meniscus edges appears to be negligible and was only noticeable over much longer times than the duration over which the experiments were conducted. In the more practical case of the ported design (Fig. 1(c)), the evaporative losses are, in any case, replaced by the working fluid. In future implementations, evaporation can be further reduced and almost completely eliminated through an enclosure with a micron-order gap along the SAW aperture to avoid absorption losses.

The maximum flow rate of order 1 ml min^{-1} reported here would seem favorable compared with other micropumps.[3] However, we note that it is slightly misleading to evaluate the pump performance solely on the maximum flow rate given its dependence on the load resistance. A review by Iverson et al. (2008) divides maximum flow rate by outlet area to allow a more meaningful comparison, in this case, yielding a value of 600 µl min^{-1} mm^{-2} which lies in the upper range of the reported values.[5] The disadvantage with pumps based on acoustic streaming, nevertheless, is the low pressures that are available,[4] here measured to be ~10 Pa including losses, to a theoretical maximum of $O(100 \text{ Pa})$:[29] many micropumps are shown to operate in the kPa range.[3–5,41] However, the use of acoustic streaming avoids many of the practical issues experienced by other technologies such as the durability of moving parts in valved reciprocating pumps and the permittivity and conductivity requirements of electrokinetic pumps.[5]

Much interest[38,39,42,43] has been paid to the valveless reciprocating pump first reported by Stemme & Stemme (1993), which utilizes kHz-order vibration of a PZT element to generate oscillatory flow through carefully designed diffuser 'valves' which act as flow rectifiers, producing a non-zero time-averaged flow.[31] The valveless pump produces kPa

pressures at ml min^{-1} flow rates and has no moving parts. As such, it is perhaps the most promising micropump to date. The disadvantage of this type of pump, however, lies in the complex geometry required for stable and efficient diffusers and the high voltages required to drive the PZT element—up to 800 V in some cases.[37]

In contrast, the advantage of using SAW as a pumping technology, in addition to the low voltages and powers required, lies in the simplicity of its design and fabrication procedure: though the performance of valveless reciprocating pumps is clearly superior, SAW pumps utilize planar transducers fabricated using standard photolithography[29,30] and are thus highly conducive to mass production. Additionally, SAW devices can easily be scaled down by reducing the finger periodicity of the interdigital transducers, increasing the frequency of operation and consequently reducing the length of the acoustic beam according to eqn (1). Thin-film SAW transducers further permit the technology to be embedded on a range of surfaces—even to flexible polymers.[44] These advantages show great promise in enabling the future development of highly complex and integrated lab-on-a-chip technology serviced by a network of numerous interconnected SAW-driven pumps and process chambers.

6 Conclusions

We have developed and characterized a SAW actuation platform that directly transmits the acoustic energy from a SAW device to a fluid actuation chamber, thus eliminating the need to transmit the wave through a coupling layer and avoiding substantial energy losses due to reflection and dissipation of the wave. The device has been employed to demonstrate rapid continuous transfer of fluid between independent reservoirs, which, to our best knowledge, is the first time this has been shown for SAW pumps. Additionally, we have characterized the SAW pump response by calculating the pressure–flow rate relationship for the system, whose linearity implies the existence of an optimal operating load resistance at which power transfer is maximized. The linear pressure–flow rate relationship also implies that the behavior of the acoustofluidic interaction within the beam chamber is relatively independent of variations in the load resistance. Further, the efficiency of the SAW pump has been found to increase with input power and with constriction of the chamber geometry, attributed to the increased shear stress within the chamber at higher flow rates and smaller cross-sectional area, therefore minimizing flow recirculation within the beam chamber. This has led to an order-of-magnitude improvement in the pumping efficiency compared to previous SAW pumps that have been reported in the literature to date.

Acknowledgements

References

1 H. Stone, A. Stroock and A. Ajdari, *Annu. Rev. Fluid Mech.*, 2004, **36**, 381–411.

2 T. Squires and S. R. Quake, *Rev. Mod. Phys.*, 2005, 77, 977–1026.

3 D. J. Laser and J. G. Santiago, *J. Micromech. Microeng.*, 2004, **14**, R35–R64.

4 P. Woias, *Sens. Actuators, B*, 2005, **105**, 28–38.

5 B. D. Iverson and S. V. Garimella, *Microfluid. Nanofluid.*, 2008, **5**, 145–174.

6 M. Madou, J. Zoval, G. Jia, H. Kido, J. Kim and N. Kim, *Annu. Rev. Biomed. Eng.*, 2006, **8**, 601–628.

7 A. Streets and Y. Huang, *Biomicrofluidics*, 2013, 7, 011302.

8 L. Yeo, H.-C. Chang, P. Chan and J. R. Friend, *Small*, 2011, 7, 12–48.

9 L. Yeo and J. R. Friend, *Biomicrofluidics*, 2009, 3, 012002.

10 Y. Fu, J. Luo, X. Du, A. Flewitt, Y. Li, G. Markx, A. Walton and W. Milne, *Sens. Actuators, B*, 2010, **143**, 606–619.

11 T.-D. Luong and N.-T. Nguyen, *Micro Nanosyst.*, 2010, **2**, 217–225.

12 J. Friend and L. Yeo, *Rev. Mod. Phys.*, 2011, **83**, 647–704.

13 Z. Wang and J. Zhe, *Lab Chip*, 2011, **11**, 1280–1285.

14 S.-C. Lin, X. Mao and T. Huang, *Lab Chip*, 2012, **12**, 2766–2770.

15 M. B. Dentry, L. Y. Yeo and J. R. Friend, *under review*, 2013.

16 R. J. Shilton, L. Y. Yeo and J. R. Friend, *Sens. Actuators, B*, 2011, **160**, 1565–1572.

17 T. Franke, A. R. Abate, D. A. Weitz and A. Wixforth, *Lab Chip*, 2009, **9**, 2625–2627.

18 R. P. Hodgson, M. Tan, L. Yeo and J. Friend, *Appl. Phys. Lett.*, 2009, **94**, 024102.

19 Y. Bourquin, J. Reboud, R. Wilson and J. Cooper, *Lab Chip*, 2010, **10**, 1898–1901.

20 Y. Bourquin, R. Wilson, Y. Zhang, J. Reboud and J. Cooper, *Adv. Mater.*, 2011, **23**, 1458–1462.

21 S. Shiokawa, Y. Matsui and T. Moriizumi, *Jpn. J. Appl. Phys.*, 1989, **28-S1**, 126–128.

22 T. Uchida, T. Suzuki and S. Shiokawa, *Proc.-IEEE Ultrason. Symp.*, 1995, 1081–1084.

23 A. Renaudin, P. Tabourier, V. Zhang, J. Camart and C. Druon, *Sens. Actuators, B*, 2006, **113**, 389–397.

24 X. Y. Du, Y. Q. Fu, J. K. Luo, A. J. Flewitt and W. I. Milne, *J. Appl. Phys.*, 2009, **105**, 024508.

25 M. Cecchini, S. Girardo, D. Pisignano, R. Cingolani and F. Beltram, *Appl. Phys. Lett.*, 2008, **92**, 104103.

26 L. Masini, M. Cecchini, S. Girardo, R. Cingolani, D. Pisignano and F. Beltram, *Lab Chip*, 2010, **10**, 1997–2000.

27 M. Travagliati, G. De Simoni, C. Lazzarini, V. Piazza, F. Beltram and M. Cecchini, *Lab Chip*, 2012, **12**, 2621–2624.

28 A. Rezk, O. Manor, J. Friend and L. Yeo, *Nat. Commun.*, 2012, **3**, 1167.

29 L. Schmid, A. Wixforth, D. Weitz and T. Franke, *Microfluid. Nanofluid.*, 2011, **12**, 229–235.

30 S. M. Langelier, L. Y. Yeo and J. Friend, *Lab Chip*, 2012, **12**, 2970–2976.

31 E. Stemme and G. Stemme, *Sens. Actuators, A*, 1993, **39**, 159–167.

32 Y. Hsu and N. Le, *Microfluid. Nanofluid.*, 2009, 7, 237–248.

33 J. Lighthill, *J. Sound Vib.*, 1978, **61**, 391–418.

34 J. J. Markham, R. T. Beyer and R. B. Lindsay, *Rev. Mod. Phys.*, 1951, **23**, 353–411.

35 D. Royer, E. Dieulesaint and D. Morgan, *Elastic Waves in Solids I: Free and Guided Propagation*, Springer, 2000.

36 P. Tabeling, *Introduction to Microfluidics*, Oxford University Press, 2005.

37 H. J. Sheen, C. J. Hsu, T. H. Wu, C. C. Chang, H. C. Chu, C. Y. Yang and U. Lei, *Microfluid. Nanofluid.*, 2007, **4**, 331–342.

38 M. Nabavi, *Microfluid. Nanofluid.*, 2009, 7, 599–619.

39 S. Wang, X. Huang and C. Yang, *Microfluid. Nanofluid.*, 2010, **8**, 549–555.

40 G. K. Batchelor, *An Introduction to Fluid Dynamics*, Cambridge University Press, 1967.

41 T. Hasegawa, J. Friend, K. Nakamura and S. Ueha, *Jpn. J. Appl. Phys.*, 2005, **44**, 4658–4661.

42 A. Ullmann, *Sens. Actuators, A*, 1998, **69**, 97–105.

43 I. Izzo, D. Accoto, A. Menciassi, L. Schmitt and P. Dario, *Sens. Actuators, A*, 2007, **133**, 128–140.

44 H. Jin, J. Zhou, X. He, W. Wang, H. Guo, S. Dong, D. Wang, Y. Xu, J. Geng, J. K. Luo and W. I. Milne, *Sci. Rep.*, 2013, **3**, 2140.